This article was downloaded by: [The Nasa Goddard Library]
On: 06 September 2012, At: 10:38
Publisher: Taylor & Francis
Informa Ltd Registered in England and Wales Registered Number: 1072954 Registered office: Mortimer House, 37-41 Mortimer Street, London W1T 3JH, UK

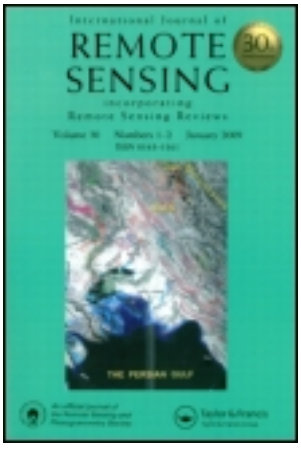

International Journal of Remote Sensing
Publication details, including instructions for authors and subscription information:
http://www.tandfonline.com/loi/tres20

Enhancement of a fire-detection algorithm by eliminating solar contamination effects and atmospheric path radiance: application to MODIS data

Liming He [a b] & Zhanqing Li [a c]

[a] Department of Atmospheric and Oceanic Science and Earth System Science Interdisciplinary Center, University of Maryland, College Park, Maryland, 20740, USA

[b] Department of Geography and Program in Planning, University of Toronto, Toronto, ON, Canada

[c] State Laboratory of Earth Surface Process and Resource Ecology, College of Global Change and Earth System Science, Beijing Normal University, Beijing, PR China

Version of record first published: 02 Aug 2011

To cite this article: Liming He & Zhanqing Li (2011): Enhancement of a fire-detection algorithm by eliminating solar contamination effects and atmospheric path radiance: application to MODIS data, International Journal of Remote Sensing, 32:21, 6273-6293

To link to this article: http://dx.doi.org/10.1080/01431161.2010.508057

PLEASE SCROLL DOWN FOR ARTICLE

Full terms and conditions of use: http://www.tandfonline.com/page/terms-and-conditions

This article may be used for research, teaching, and private study purposes. Any substantial or systematic reproduction, redistribution, reselling, loan, sub-licensing, systematic supply, or distribution in any form to anyone is expressly forbidden.

The publisher does not give any warranty express or implied or make any representation that the contents will be complete or accurate or up to date. The accuracy of any instructions, formulae, and drug doses should be independently verified with primary

sources. The publisher shall not be liable for any loss, actions, claims, proceedings, demand, or costs or damages whatsoever or howsoever caused arising directly or indirectly in connection with or arising out of the use of this material.

Downloaded by [The Nasa Goddard Library] at 10:38 06 September 2012

International Journal of Remote Sensing
Vol. 32, No. 21, 10 November 2011, 6273–6293

Downloaded by [The Nasa Goddard Library] at 10:38 06 September 2012

Enhancement of a fire-detection algorithm by eliminating solar contamination effects and atmospheric path radiance: application to MODIS data

LIMING HE†‡ and ZHANQING LI*†§
†Department of Atmospheric and Oceanic Science and Earth System Science Interdisciplinary Center, University of Maryland, College Park, Maryland 20740, USA
‡Department of Geography and Program in Planning, University of Toronto, Toronto, ON, Canada
§State Laboratory of Earth Surface Process and Resource Ecology, College of Global Change and Earth System Science, Beijing Normal University, Beijing, PR China

(*Received 5 April 2010; in final form 9 July 2010*)

Traditional fire-detection algorithms with either fixed or contextual thresholds mainly rely on the temperature contrast between a fire pixel and its surrounding pixels in the mid-infrared (MIR) and thermal-infrared (TIR) bands. Solar contamination and thermal atmospheric path radiance in the MIR band can weaken the contrast between the high- and low-temperature objects and undermine the capability of detecting fires during daytime. The degree of solar contamination in the MIR band depends on variable surface albedo, solar zenith angle and atmospheric conditions. A method is proposed to eliminate the solar radiation and thermal path radiance received by the MODerate Resolution Imaging Spectroradiometer (MODIS) sensor in the MIR band. The modified MIR brightness temperature is incorporated into the existing fire-detection algorithm (referred to as 'MOD14') after re-tuning the daytime thresholds. The performance of the revised algorithm (referred to as 'MOD-MOD') was tested using coincident data from the Advanced Spaceborne Thermal Emission and Reflection Radiometer (ASTER) onboard the Terra satellite and visual inspection of large quantities of MODIS imageries. Moderate improvements are achieved in the detection rate while retaining low commission errors. Improvement of the detection by MOD-MOD depends on land-cover type. The majority of the false detections occur over deforested area.

1. Introduction

Wildfires emit large amounts of trace gases and aerosol particles into the atmosphere (Ichoku and Kaufman 2005), modify landscape and vegetation patterns, and thus play an important role in the Earth's ecosystems and climate (Beringer *et al.* 2003, Jin and Roy 2005). Currently, remote sensing is one of the most effective methods to detect active fires, especially over a vast territory of remote regions (Kaufman *et al.* 1998, Li *et al.* 2001). Fires can drastically reduce surface solar radiation budget and thus affect regional climate (Masuda *et al.* 1995, Li 1998).

*Corresponding author. Email: zli@atmos.umd.edu

International Journal of Remote Sensing
ISSN 0143-1161 print/ISSN 1366-5901 online © 2011 Taylor & Francis
http://www.tandf.co.uk/journals
http://dx.doi.org/10.1080/01431161.2010.508057

In general, there are two types of algorithms that use mid-infrared (MIR) and thermal-infrared (TIR) data to detect active fires: the fixed-threshold algorithm and the contextual algorithm. The fixed-threshold algorithm has the best performance for regional and unique landscapes (Kaufman *et al.* 1990, Kennedy *et al.* 1994, Li *et al.* 1997, Li *et al.* 2000a,b). In contrast, the contextual algorithm uses dynamic thresholds, and thus is more applicable to variable surface conditions (Lee and Tag 1990, Flasse and Ceccato 1996, Nakayama *et al.* 1999, Giglio *et al.* 2003, Lasaponara *et al.* 2003, Wang *et al.* 2007). Large discrepancies exist among different fire algorithms and fire products (Ichoku *et al.* 2003).

Despite a variety of algorithms and sensors used in fire detection, large errors, including both commission and omission errors, still exist due to various limitations and uncertainties, such as contamination due to solar reflected radiation and saturation in the MIR channel, cloud screening, unequal atmospheric effects between spectral bands and observation angles (Giglio and Kendall 1999, Li *et al.* 2001, Csiszar and Sullivan 2002, Wang *et al.* 2007).

Radiance received by a sensor in the MIR band originates from both thermal emission and solar reflection, while fire detection relies on the contrast in thermal emission (Boyd and Petitcolin 2004). Usually, surfaces with different natural characteristics (e.g. albedo/emissivity and thermal inertia) are heated unevenly in the daytime. Therefore, the spatial temperature differences in the daytime for different objects are larger compared to nighttime data (Verstraeten *et al.* 2006, Rowlands and Sarris 2007). The solar radiation reflected and scattered by the ground and atmosphere in the MIR band (referred to as 'solar contamination' hereafter), depends on the surface albedo, solar and viewing geometries, the condition of the atmosphere, etc. As far as fire detection is concerned, these factors undermine the detection performance for those algorithms, and such factors are not considered.

To tackle these problems, daytime radiative-transfer simulations were carried out in the MIR band and the effect of solar contamination was analysed. A method is proposed to correct for solar contamination, and this method is applied to the MODerate Resolution Imaging Spectroradiometer (MODIS) fire-detection algorithm (Giglio *et al.* 2003) to improve its fire-detection capability. The thermal path radiance is also taken into account to further improve the algorithm.

The following section describes the data used. Section 3 describes the principle and methodology. A detailed evaluation of the modified algorithm is given in section 4 and section 5 is a summary of the study.

2. Datasets

Data employed in this study include MODIS data and Advanced Spaceborne Thermal Emission and Reflection Radiometer (ASTER) data. The MODIS level 1B calibrated radiance 1 km data (MOD021 km or MYD021 km), together with the MODIS 1 km geolocation data (MOD03, or MYD03), were used to produce the MODIS level 2 fire and thermal anomalies product (MOD14, or MYD14). The MODIS radiance and geolocation data were derived from collection 5.

A total of 81 MODIS granules were matched with 115 coincident ASTER scenes over the US from 2002 to 2006 (Schroeder *et al.* 2008b) for algorithm refinement. Another 135 MODIS granules coincident with 162 ASTER scenes were used for algorithm validation. These scenes were mainly located over the deforestation region of Amazonia from 2000 to 2005 (Schroeder *et al.* 2008a). In addition, 2695 MODIS

Downloaded by [The Nasa Goddard Library] at 10:38 06 September 2012

Table 1. The MODIS bands used in the algorithm.

Channel number	Central wavelength (μm)	Denotation	Purpose
1	0.65	$\rho_{0.65}$	Sun glint and coastal false-alarm rejection; cloud masking
2	0.86	$\rho_{0.86}$	Bright surface, sun glint and coastal false-alarm rejection; cloud masking
7	2.1	$\rho_{2.1}$	Sun glint and coastal false-alarm rejection
21	4.0	T_4	High-range channel for active fire detection
22	4.0	T_4	Low-range channel for active fire detection
31	11.0	T_{11}	Active fire detection, cloud masking
32	12.0	T_{12}	Cloud masking

Downloaded by [The Nasa Goddard Library] at 10:38 06 September 2012

granules from July 2004 and 2384 MODIS granules from August 2005 over North America were processed to generate fire products with the MODIS original and modified algorithms. Qualitative assessment of the fire products was also carried out by visual inspection of fire smoke plumes. A total of 619 granules in July 2004 and 543 granules in August 2005 were found to contain at least one fire. A summary of the MODIS bands used in the fire-detection algorithm is listed in table 1 (Giglio *et al.* 2003).

The MODIS land-surface temperature/emissivity monthly L3 global 0.05° climate model grid (CMG) product (MOD11C3, collection 5) for the whole period from 2000 to 2006 (Wan and Li 1997) and the MOD12Q1 V004 land-cover product (in 0.008333° resolution, collection 4) from 2001 to 2004 were used to produce the surface emissivity at 0.008333° resolution (Friedl *et al.* 2002). These data were downloaded from the Earth Observing System (EOS) Data Gateway and the Land Processes Distributed Active Archive Center (DAAC) (Justice *et al.* 2002b). The MOD12Q1 collection 5 product has fine spatial resolution (500 m), but was unavailable at the time of this study.

While the principle of the new fire-detection approach is demonstrated with MODIS data, the methodology is sound for any fire sensor. However, algorithm modifications are specific to each sensor due to their different characteristics, especially the spectral band and number of channels and spectral response functions, as shown in figure 1 for the widely used MODIS and Advanced Very High Resolution Radiometer (AVHRR) sensors and the Advanced Baseline Imager (ABI) sensor aboard the future Geostationary Operational Environmental Satellite-R (GOES-R) satellite.

3. Solar contamination and its elimination

3.1 *The principle*

Radiance received in an MIR channel under clear-sky conditions consists of two parts: the thermal radiance, L_{emit}, emitted from the atmosphere and ground surface and the solar radiation, L_{sun}, resulting from the scattering/reflection of the atmosphere

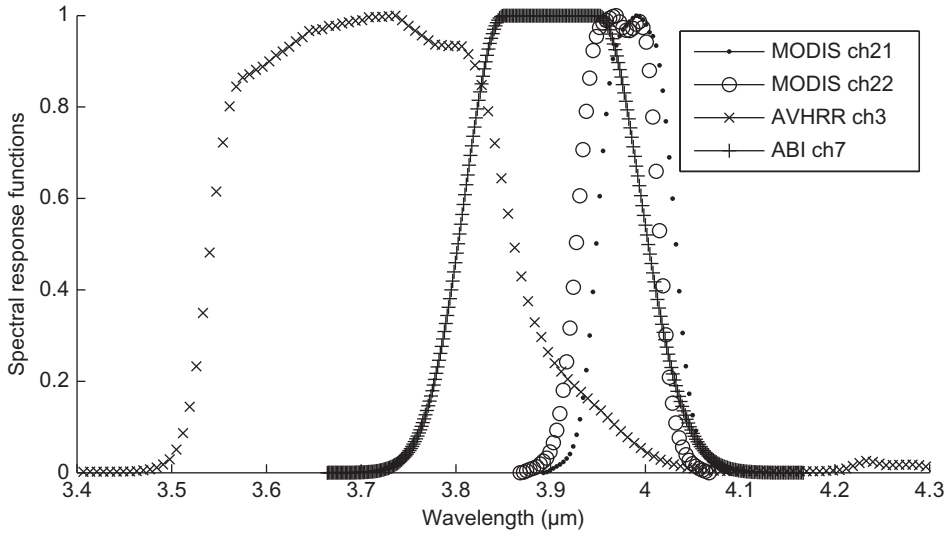

Figure 1. Spectral response functions for MODIS ch21/22, ABI ch7 and AVHRR ch3.

and surface (Wan and Li 1997). Omitting the wavelength and angle notations for simplification and assuming a Lambertian ground surface, this can be expressed as:

$$L = L_{\text{emit}} + L_{\text{sun}}, \tag{1}$$

where

$$L_{\text{emit}} = L_{\text{a}} + L_{\text{g}} \tag{2}$$

and

$$L_{\text{sun}} = L_{\text{s}} + \frac{\alpha}{\pi\,(1-\alpha S)}\mu_{\text{s}} E_0\,[t_{\text{s}} + t_{\text{ds}}]\,[t_{\text{v}} + t_{\text{dv}}]\,. \tag{3}$$

In equation (2), L_{a} is the thermal path radiance and L_{g} is the thermal radiance from the ground surface. In equation (3), L_{s} is the path radiance resulting from the scattering of solar radiation by the atmosphere; α is the surface albedo ($\alpha = 1 - \varepsilon_{\text{v}}$) and ε_{v} is the surface emissivity; S is the spherical albedo of the atmosphere; μ_{s} is the cosine of the solar zenith angle; E_0 is the solar irradiance incident at the top of the atmosphere and measured in a plane perpendicular to the rays; t_{s} is the transmission function for the solar beam; t_{ds} is the transmission function for the downward diffuse solar radiation; t_{v} is the direct transmission function between the surface and the sensor; and t_{dv} is the transmission function for the upward diffuse solar radiation. To compute the brightness temperature, T_{b}, in an MIR band, from radiance L:

$$T_{\text{b}} = B'\,(L, \lambda)\,, \tag{4}$$

where B' ( ) is the inverse of the Planck function in the MODIS band (λ) given by:

$$T_{\text{b}} = \frac{c_2}{\lambda \log\left(1 + \frac{c_1}{L\lambda^5}\right)}, \tag{5}$$

Downloaded by [The Nasa Goddard Library] at 10:38 06 September 2012

where L is in W m^{-2}sr^{-1} μm^{-1}, $c_1 = 1.19107 \times 10^8$ W μm^4 m^{-2} sr^{-1} and $c_2 = 1.43883 \times 10^4$ μm K. In simulating satellite-observed radiances, the radiance needs to be integrated over the bandpass of the sensor weighted by the spectral response function of the sensor.

The essential information pertaining to fire detection is conveyed in $T_g = B'(L_g, \lambda)$, but current fire-detection algorithms employ the brightness temperature given by equation (4), which is influenced by non-fire-related contributions of solar reflection and atmospheric path radiances. As demonstrated by Li *et al.* (2001), the relative contribution of solar reflection to the total MIR radiance depends primarily on surface albedo, temperature and the solar zenith angle. Using the MODTRAN4 model (Berk *et al.* 1998), we computed T_b for various values of the above influential variables. Figure 2 shows the effect of solar radiation reflected from a 100% Lambertian ground surface expressed as an equivalent blackbody temperature (T_0). The effect of solar radiation is the largest for AVHRR band 3, smallest for MODIS bands (21 and 22) and intermediate for the future GOES-R ABI band 7. In addition, T_0 decreases with increasing solar zenith angle. Figure 3 shows the change in brightness temperature after the elimination of solar radiation for some ordinary atmospheric conditions. The effect of solar contamination on fire detection depends on its absolute value and its relative quantity to the thermal emission. Solar contamination has the smallest effect when its equivalent blackbody temperature is close to the surface brightness temperature (and/or surface reflectivity is small); the temperature difference can reach 40 K for highly reflective surfaces and cooler targets.

Figure 4 illustrates how the solar contamination can cause omission errors. Considering a group of pixels that have similar surface temperatures, the fire in the central pixel increases brightness temperature in the MIR band. Assuming that the contrast in brightness temperature between the fire pixel and its neighbourhood just

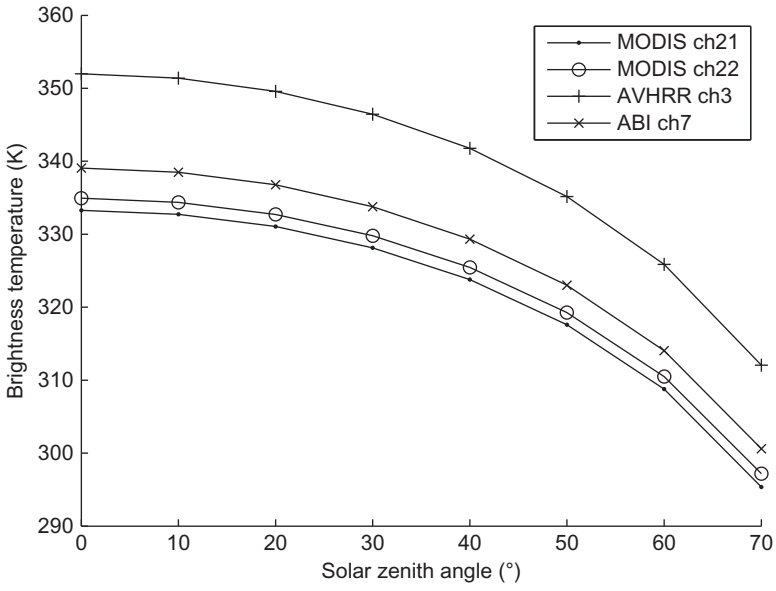

Figure 2. The equivalent blackbody temperature (T_0) of reflected solar radiation by a 100% Lambertian ground surface for the mid-latitude atmosphere model ($L = B(T_0) = S_0 t_s \mu_s / \pi$).

Downloaded by [The Nasa Goddard Library] at 10:38 06 September 2012

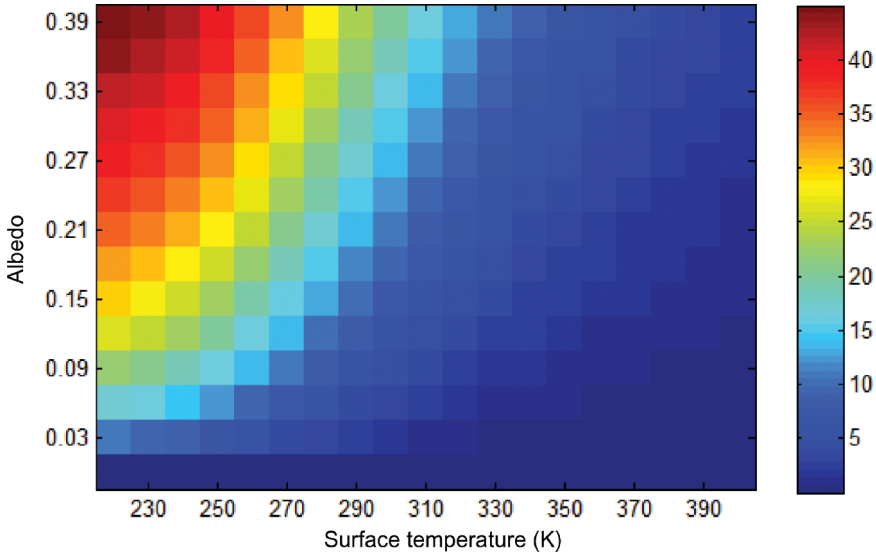

Figure 3. Brightness-temperature differences (in K) before and after the elimination of solar contamination for varying surface temperatures and albedos (mid-latitude summer atmosphere, column water vapour = 2.9 cm, solar zenith angle = 45°, viewing zenith angle = 0°, visibility = 23 km).

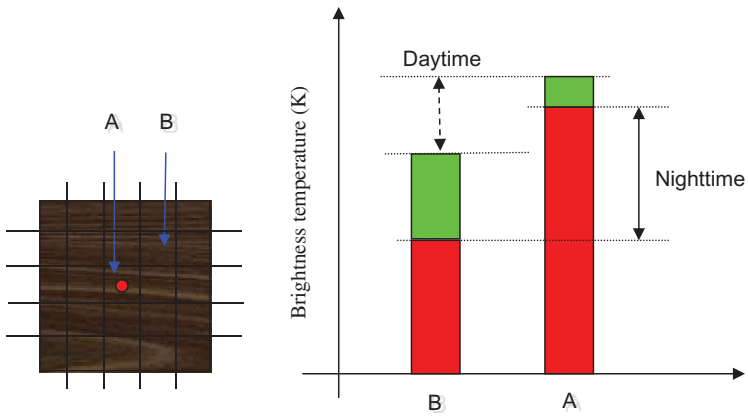

Figure 4. Demonstration of solar contamination causing omission errors. Pixel A contains a fire, and pixel B represents the background. The red bar denotes the brightness temperatures at night, and the green bar denotes the increases in brightness temperatures by adding the same amount of solar radiation to different thermal environments during daytime. The length of the solid arrow denotes the contrast of brightness temperature during nighttime, while the dotted arrow is the same but during daytime. The contrast between fire and non-fire pixels is reduced from nighttime to daytime due to solar contamination.

reaches the thresholds, this fire would just be detected by a fire algorithm if there were no solar radiation. Adding the same amount of solar contamination to a hotter fire pixel would elevate the brightness temperature by a less amount than a colder non-fire pixel due to the nonlinear inversion function. Pixels of high surface temperatures (e.g.

Downloaded by [The Nasa Goddard Library] at 10:38 06 September 2012

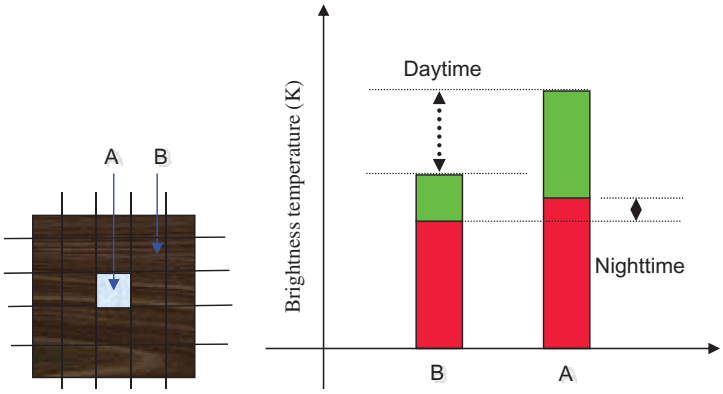

Figure 5. Demonstration of solar contamination causing commission errors. Pixel A is a high-reflective object, and pixel B denotes the low-reflective background. The red bars denote nighttime brightness temperatures, which are similar, and the green bars denote increases in brightness temperatures by adding different amounts of solar radiation during daytime. The length of the solid arrow denotes the contrast in brightness temperature during nighttime, and the length of the dotted arrow is the same but for daytime. The contrast between the bright pixel and its neighbourhood pixels is increased due to different amounts of solar radiation.

Downloaded by [The Nasa Goddard Library] at 10:38 06 September 2012

fires) have smaller increases in brightness temperature than those of low surface temperatures (background). As a result, the contrast in brightness temperature is likely reduced so much that the fire may not be detected, as shown in figure 4.

The solar contamination can also cause commission errors, as demonstrated in figure 5. Assuming a high reflective object is surrounded by low reflective scenes, without burning, their temperature contrast is usually so small during nighttime that it does not trigger a fire detection. During daytime, however, the higher reflective object may reflect much more solar energy than the lower reflective object, so that the brightness-temperature contrast is enhanced enough to exceed the threshold, rendering a commission error.

Thermal path radiance has a similar effect as that of solar contamination on fire-detection algorithms. Different changes in the brightness temperature of a pixel can occur due to different atmospheric path radiance. The thermal path radiance depends on the viewing zenith angle: the larger the viewing zenith angle, the greater the thermal path radiance.

3.2 *Elimination of solar contamination in the MIR band*

Surface thermal radiance can be obtained by subtracting both the reflected solar radiance and atmospheric radiance from the total radiance:

$$L_{\text{emit}} = L - L_{\text{sun}} - L_{\text{a}}. \tag{6}$$

A modified brightness temperature, $T_{4\text{m}}$, in the MIR band can be expressed as:

$$T_{4\text{m}} = B'\left(L_{\text{emit}}\right). \tag{7}$$

To this end, L_{sun}, L_a and their components (L_s, S, t_s, t_v, t_{ds} and t_{dv}) are computed using the MODTRAN4 model with a variety of atmospheric and surface parameters and varying viewing geometries. The output data are then used to develop look-up tables (LUTs) for speedy application. To separate the solar and thermal components, the model is run twice for every case, with and without solar radiation. To isolate atmospheric components, the ground albedo and absolute temperature are both set to zero. After the LUT is built, multi-dimensional linear interpolation is used to estimate any of the six parameters. The LUT has four dimensions for the mid-latitude summer atmosphere model (visibility 23 km): surface elevation (H), viewing zenith angle (θ_v), solar zenith angle (θ_s) and relative azimuth angle (ϕ). The surface elevation ranges from 0 to 4.0 km at an interval of 0.4 km. The intervals for viewing and solar zenith angles are 5° from 0° to 75°. The interval for the relative azimuth angle is 20° from 0° to 180°. L_s is a function of H, θ_v, θ_s and ϕ; S is a function of H; and t_s, t_v, t_{ds} and t_{dv} are functions of the solar (viewing) angle and H.

It is worth noting that the MIR band is insensitive to most atmospheric variables that affect general radiative transfer in the atmosphere, such as ozone, water vapour and aerosols (King *et al.* 2003, Seemann *et al.* 2003, Remer *et al.* 2005). Ozone has no absorption band in the MIR region. The aerosol effect in the MIR band is almost negligible, especially for fine-mode smoke aerosols produced by fires (Kaufman and Remer 1994). As per our sensitivity tests, use of the rural aerosol model for visibilities ranging from 23 to 5 km leads to a relative variation of solar radiation recorded by MODIS in the MIR band of less than 3%. Use of the mid-latitude summer atmosphere with water-vapour amounts ranging from 0 to 4 g cm^{-2} results in a variation of solar radiation recorded by the MODIS MIR band of less than 2%.

Thermal path radiance in the MIR band, L_a, mainly depends on surface elevation, satellite viewing zenith angle and atmospheric temperature profiles. There is a MODIS atmospheric profile product, but it was not used in this demonstration study. Since the thermal path radiance is generally much smaller than the solar reflectance in the MIR band, the atmospheric profile data are taken from the mid-latitude summer atmosphere model and are used to generate the LUT.

3.3 *Determination of surface emissivity/albedo*

In this study, a Lambertian surface albedo (of emissivity equal to one) is assumed in the MIR band. The MOD11C3 emissivity product at monthly CMG was used to produce albedo data in our algorithm (Wan and Li 1997). The emissivity data are given at 0.05° latitude/longitude (~5 km). Re-sampling is performed to derive higher resolution (1 km) data from the lower resolution data with the help of higher resolution (1 km) land-cover data. The emissivity of a 0.05° pixel is assumed to be a linear combination of the emissivities of discrete land-cover types as specified by the 6 × 6 0.008333° land-cover types, with weighting coefficients determined by the percentages of pixels of the same land-cover types.

Re-sampling was done by first selecting the 6 × 6 array of emissivity pixels possessing a homogeneous land-cover type (see table 2). Then the ratio, c, was calculated for every 0.05° pixel:

$$c = \frac{E}{\tilde{E}}, \tag{8}$$

Downloaded by [The Nasa Goddard Library] at 10:38 06 September 2012

Table 2. Emissivities of uniform pixels at 0.05° resolution for International Geosphere-Biosphere Programme (IGBP) land-cover types. MODIS emissivity data (MOD11C3) in July 2004 are used.

ID	IGBP type	Samples	Mean	Standard deviation
0	Water	128 432	0.95	0.025
1	Evergreen needleleaf forest	33 555	0.95	0.006
2	Evergreen broadleaf forest	233 147	0.96	0.008
3	Deciduous needleleaf forest	4440	0.94	0.008
4	Deciduous broadleaf forest	2160	0.94	0.009
5	Mixed forests	17 682	0.94	0.007
6	Closed shrublands	274	0.93	0.013
7	Open shrublands	305 988	0.92	0.034
8	Woody savannas	6379	0.94	0.015
9	Savannas	6541	0.92	0.024
10	Grasslands	111 365	0.92	0.017
11	Permanent wetlands	4	0.95	0.012
12	Croplands	149 409	0.95	0.009
13	Urban and built up	2836	0.95	0.018
14	Corpland/natural vegetation	512	0.94	0.011
15	Snow and ice	45 909	0.98	0.005
16	Barren or sparsely vegetated	492 019	0.86	0.044
17	Unclassified	4	0.93	0.007

where E is the 0.05° emissivity and $\tilde{E}$ is the mean emissivity of the corresponding 6×6 pixels. The latter is given by:

$$\tilde{E} = \sum_{i=1}^{n} E_{wi}/n, \tag{9}$$

where n is the number of pixels with a valid land-cover type. The weighted emissivity for a land-cover type, E_{wi}, is expressed as:

$$E_{wi} = \frac{\sum_{j=1}^{m} w_j E_{i,j}}{\sum_{j=1}^{m} w_j}, \tag{10}$$

where $E_{i,j}$ is the jth emissivity near the centre pixel for land-cover type i (see table 2). The total number of pixels to be selected from the neighbourhood for a particular land-cover type i is denoted as m, and $w_j = 1/D_j^2$, where D_j is the distance between the centre pixel and the selected pixel. The parameter m is selected according to the available computational resources and acceptable runtime. The final emissivity of a 1 km pixel within the 6×6 region is calculated as:

$$e = cE_{wi}. \tag{11}$$

The selection of the adjacent pure pixel to calculate emissivity for a land-cover type is based on the 'first law of geography' (Tobler 1970).

Downloaded by [The Nasa Goddard Library] at 10:38 06 September 2012

4. Modification and testing of the fire-detection algorithms

After removing the reflected solar radiance and thermal path radiance, the original MODIS fire-detection algorithm (referred to as 'MOD14' hereafter) is modified to improve fire detection. Coincident active fires detected by ASTER have been used for validation of the MODIS fire product (Morisette *et al.* 2005, Csiszar *et al.* 2006, Schroeder *et al.* 2008a). In this study, we employed 131 ASTER scenes matched with 81 MODIS granules in the United States (Schroeder *et al.* 2008b) for algorithm modification, while an independent matched dataset in Amazonia is used for testing (same dataset used by Schroeder *et al.* (2008a)). Active fire masks for ASTER scenes were produced using ASTER channels 3 and 8 based on a contextual approach. The MODIS fire product was overlaid on top of the ASTER fire masks using the Terra MODIS geolocation product. The sum of 30 m active fire masks was used to assess omission and commission errors for each MODIS pixel sampled.

The MOD-MOD algorithm was modified to achieve maximum-true-fires, while keeping the number of false fires in the same level as the original algorithm. The MOD14 works on both daytime and nighttime pixels (Giglio *et al.* 2003). Only the daytime algorithm is tested here. In the original version of the algorithm, daytime is defined when the solar zenith angle (θ_s) is less than 85°. In the modified algorithm (referred to as 'MOD-MOD' hereafter), daytime is redefined as having $\theta_s \leq 75°$ to avoid large errors incurred in radiative-transfer calculations for large solar zenith angles (Berk *et al.* 1998).

The MODIS fire-detection algorithm consists of a series of tests (filters) as listed in table 3. $\Delta T_m = T_{4m} - T_{11}$ and values in $\langle\rangle$ brackets represent thresholds to be tuned. Two different sets of threshold values (A through to F in table 3) are given in table 4 representing the official EOS National Aeronautics and Space Administration (NASA) fire algorithm (MOD14) and modified algorithm (MOD-MOD). In the MOD-MOD algorithm, the values of T_4, ΔT, $\overline{T}_4$, $\overline{\Delta T}$, δ_{T_4} and $\delta_{\Delta T}$ are changed to T_{4m}, ΔT_m, $\overline{T}_{4m}$, $\overline{\Delta T}_m$, $\delta_{T_{4m}}$ and $\delta_{\Delta T_m}$ after removal of the solar contamination and thermal path radiance. The scatter plots in figure 6 show the comparisons of these variables between the original and modified fire-detection algorithms. The brightness-temperature differences ($T_4 - T_{4m}$) vary from 0 to 4 K, with the mode close to 2 K. For the non-burning background pixels, the mode of differences between the mean T_4 and mean T_{4m} ($\overline{T}_4 - \overline{T}_{4m}$) is around 4 K. The decrease in MIR brightness temperature should be smaller for fire pixels than for background pixels due to the nonlinear conversion from radiance to brightness temperature. Most δ_{T_4} and $\delta_{T_{4m}}$ are less than 4 K, and most of the differences between $\delta_{T_{4m}}$ and δ_{T_4} are less than 0.5 K. Positive differences mean that the correction for solar contamination and thermal path radiance slightly increase the brightness-temperature contrast within these non-burning background pixels. The plots of ΔT versus ΔT_m and $\delta_{\Delta T}$ versus $\delta_{\Delta T_m}$ show similar distributions since brightness temperatures in the thermal band are unchanged.

To test if the modifications made to the algorithm help detect more fires, the following four residuals are defined, which are used in filter 8 in table 3:

$$R_{1m} = T_{4m} - \left(\overline{T}_{4m} + 3\delta_{T_{4m}}\right), \tag{12}$$

$$R_1 = T_4 - \left(\overline{T}_4 + 3\delta_{T_4}\right), \tag{13}$$

$$R_{2m} = \Delta T_m - \left(\overline{\Delta T_m} + 3.5\delta_{\Delta T_m}\right) \tag{14}$$

Downloaded by [The Nasa Goddard Library] at 10:38 06 September 2012

Downloaded by [The Nasa Goddard Library] at 10:38 06 September 2012

Table 3. Major steps of daytime MODIS fire-detection algorithms and modifications.

No.	Components (filters)	Criteria and thresholds
1	Water masking	Identify by the 1 km prelaunch land/sea mask contained in the MODIS geolocation product
2	Cloud masking	$(\rho_{0.65} + \rho_{0.86} > 0.9)$ or $(T_{12} < 265\text{K})$ or $(\rho_{0.65} + \rho_{0.86} > 0.7$ and $T_{12} < 285\text{K})$
3	Elimination of solar contamination and thermal path radiance	Modify the original T_4 to $T_{4\text{m}}$ by removing solar contamination and thermal path radiance
4	Potential fire identification	$T_{4\text{m}} > \langle A \rangle$ K and $\Delta T_{\text{m}} > 10\text{K}$ and $\rho_{0.86} < \langle B \rangle$
5	Absolute threshold test	$T_{4\text{m}} > \langle C \rangle$ K
6	Exclusion of fires in the background window for filter 7	$T_{4\text{m}} > \langle D \rangle$ K and $\Delta T_{\text{m}} \geq \langle E \rangle$ K
7	Statistics of background characterization	Search valid neighbouring pixels and calculate their statistics
8	Contextual test	$\Delta T_{\text{m}} > \overline{\Delta T_{\text{m}}} + \max\left(3.5\delta_{\Delta T_{\text{m}}}, \langle F \rangle\right)$ and $T_{4\text{m}} > \overline{T}_{4\text{m}} + 3\delta_{T_{4\text{m}}}$ and $(T_{11} > \overline{T}_{11} + \delta_{T_{11}} - 4\text{K}$ or $\delta_4{}' > 5\text{K})$
9	Sun-glint rejection	$\theta_{\text{g}} < 2°$ or $(\theta_{\text{g}} < 8°$ and $\rho_{0.65} > 0.1$ and $\rho_{0.86} > 0.2$ and $\rho_{2.1} > 0.12)$ or $\left(\theta_{\text{g}} < 12°\right.$ and $\left.(N_{\text{aw}} + N_{\text{w}}) > 0\right)$
10	Desert boundary rejection	$N_{\text{f}} > 0.1N_{\text{v}}$ and $N_{\text{f}} \geq 4$ and $\rho_{0.86} > 0.15$ and $\overline{T}'_{4\text{m}} < 345$ K and $\delta'_{T_{4\text{m}}} < 3\text{K}$ and $T_{4\text{m}} < \overline{T}'_{4\text{m}} + 6\delta'_{T_{4\text{m}}}$
11	Coastal false alarm	$N_{\text{uw}} > 0$ and $T_{4\text{m}} < \langle C \rangle$ K

Notes: Values in $\langle\rangle$ (A to F) are quantities for adjustment whose values are given in table 4. The number of valid pixels within the background window is denoted by N_{v}; the number of neighbouring pixels rejected as background fire is N_{f}; and the number of neighbouring pixels excluded as water is represented by N_{w}. $\overline{\Delta T}_{\text{m}}$ and $\delta_{\Delta T_{\text{m}}}$ are the respective mean and mean absolute deviations MADs of ΔT_{m}; $\overline{T}_{4\text{m}}$ and $\delta_{T_{4\text{m}}}$ are the respective mean (MEAN) and MAD of $T_{4\text{m}}$; and $\overline{T}_{11}$ and $\delta_{T_{11}}$ are the respective mean and MAD of T_{11}. $\overline{T}'_{4\text{m}}$ and $\delta'_{T_{4\text{m}}}$ are the respective mean and MAD for valid background fire pixels. In filter 9, $\cos\theta_{\text{g}} = \cos\theta_{\text{v}}\cos\theta_{\text{s}} - \sin\theta_{\text{v}}\sin\theta_{\text{s}}\sin\theta_{\phi}$, where θ_{v} and θ_{s} are the viewing and solar zenith angles and ϕ is the relative azimuth angle. N_{aw} is the number of water pixels within the eight pixels surrounding the tentative fire pixel. In filter 11, the normalized difference vegetation index, $\text{NDVI} = (\rho_{0.86} - \rho_{0.65})/(\rho_{0.86} + \rho_{0.65})$; valid background pixels have $\rho_{2.1} < 0.05$, $\rho_{0.86} < 0.15$ and $\text{NDVI} < 0$ is considered as unmasked water pixel in the land/sea mask product and the number of these pixels is denoted as N_{uw}.

Table 4. The thresholds for MOD14 and MOD-MOD algorithms.

	A	*B*	*C*	*D*	*E*	*F*
MOD14	310	0.3	360	325	20	6
MOD-MOD	300	0.35	350	305	15	7

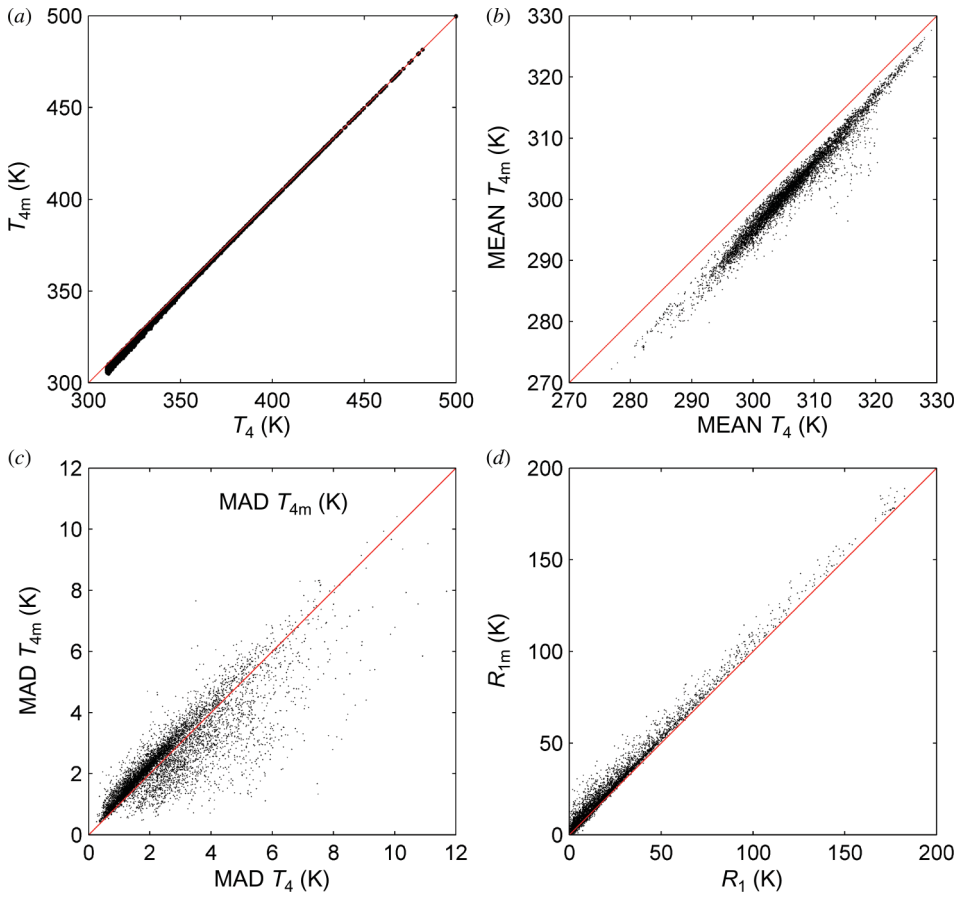

Figure 6. Scatter plots for various parameters between the MOD-MOD and MOD14 fire detection.

and

$$R_2 = \Delta T - \left(\overline{\Delta T} + 3.5\delta_{\Delta T}\right). \tag{15}$$

The larger the residuals are, the greater is the confidence that pixels are identified as true fires. It follows from the plots of R_1 versus R_{1m} and R_2 versus R_{2m} that the residuals for the new algorithm have increased for most of the fires. The increases result from the integrated effects of three factors: (1) a large decrease in background pixel temperatures; (2) a minor decrease in the fire pixel temperatures; and (3) a slight

Downloaded by [The Nasa Goddard Library] at 10:38 06 September 2012

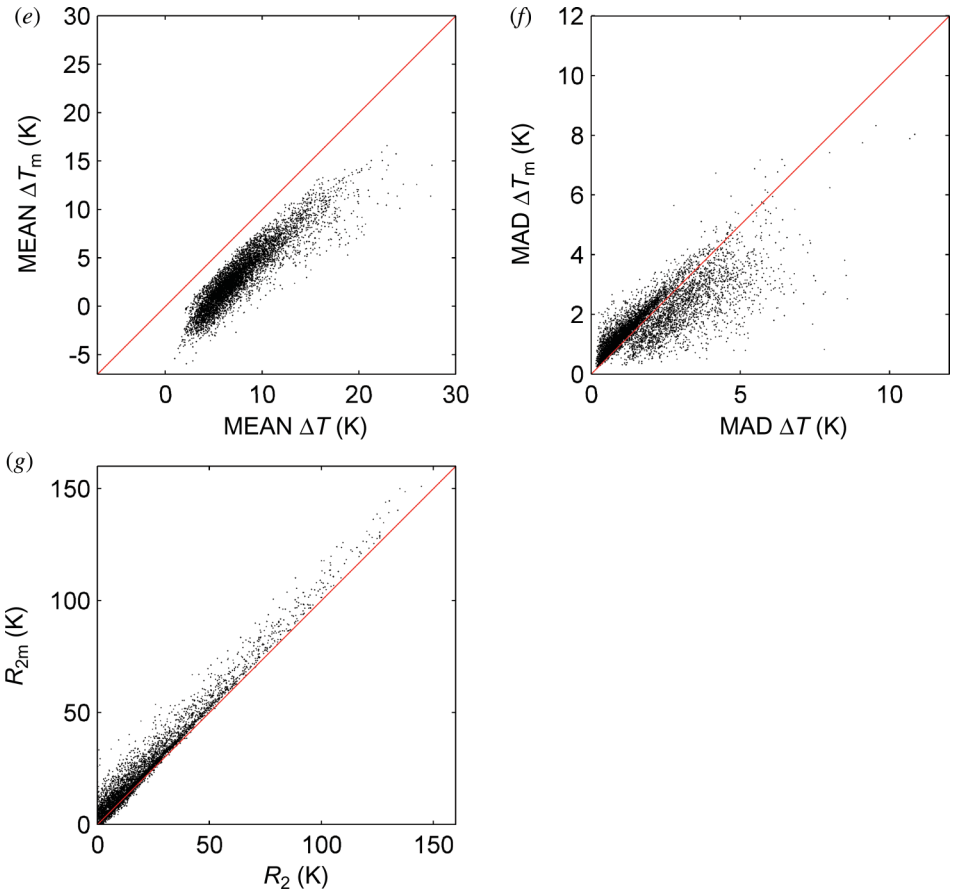

Figure 6. (*Continued*.)

increase in mean absolute deviation (MAD). These changes in the thresholds help understand the fundamental questions concerning the effectiveness of fire-detection algorithms.

The performance of the fire-detection algorithms are evaluated in terms of commission errors and omission errors relative to the ASTER-based fire product. The commission error (C) is defined as the ratio of the number of false fire pixels to the total number of fire pixels identified from ASTER fire masks for MODIS pixels, and is expressed as a percentage. False detection is defined as any MODIS fire pixel containing no ASTER active fire pixels within their footprints. The omission error (O) is defined as the ratio of the number of undetected MODIS fire pixels including at least one ASTER fire masks to the number of MODIS fire pixels that include at least one ASTER fire masks, and is also expressed as a percentage.

When applying the algorithms to the North American MODIS data (covering conterminous North America, February 2002–November 2005), the number of fires detected by the two algorithms are: 7987 for MOD14 and 9929 for MOD-MOD, a 24.3% increase. A small subset of the MODIS pixels was matched with 115 ASTER

Downloaded by [The Nasa Goddard Library] at 10:38 06 September 2012

scenes containing 418 250 MODIS pixels (all the ASTER scenes are within the conterminous US). Out of the matched pixels, 3605 MODIS pixels show at least one 30 m ASTER active fire pixel; true fires detected by the algorithms are: 642 for MOD14 and 710 for MOD-MOD, so the omission errors are 82.2% for MOD14 and 80.3% for MOD-MOD. The number of false fires is eight for both algorithms, so the commission errors are 1.23% for MOD14 and 1.11% for MOD-MOD. For those users wanting minimum-false-fires, increasing the threshold 'F' through fine tuning is a simple and effective means to lower the commission errors at the cost of missing a small number of true fires. The overall statistics of the performance for the training data are shown in figure 7.

Both algorithms were also applied to an independent dataset in Amazon. First, the algorithms were applied to 135 MODIS granules. The number of fire pixels detected by MOD14 is 90 728 and 109 510 by MOD-MOD, or 20.9% more. The difference is on a par with that obtained in North America. To evaluate the commission and omission errors for this independent dataset, 162 ASTER scenes were matched with the MODIS granules, leading to 7300 MODIS pixels containing at least one ASTER 30 m active fire mask out of ~583 200 MODIS pixels. The commission errors are 17.1% (287 false fires out of 1681 detections) for MOD14 and 17.7% (or 339 false fires out of 1920 detections) for MOD-MOD. The false detections occur mostly over fresh burns (Schroeder *et al.* 2008a). The lack of monthly updated land-cover products posed a puzzle for the MOD-MOD algorithm to remove more commission errors in the intense logging area. The average omission errors are 80.9% for MOD14 and 78.3% for MOD-MOD. The omission errors of MOD-MOD are less than or equal to the omission errors of MOD14 for all land-cover types, except for 'closed shrublands' and 'croplands'. The overall statistics of the performance for the independent test data are shown in figure 8.

The improvement of the detection accuracy by MOD-MOD seems to have a strong dependence on land-cover type (figures 7 and 8). Over the training dataset, the detection rate is improved by 22.7% in 'evergreen needleleaf forest', the improvement for other land covers is not obvious; over the validation dataset, the detection rate is improved by 20.4% in 'evergreen broadleaf forest' (with commission errors of 24.5% for MOD14 and 23.7% for MOD-MOD).

Given the highly limited ASTER scenes that can be matched with MODIS, we also visually examined 250 m MODIS imagery data (MOD02QKM or MYD02QKM) for spotting fire events based on smoke plums/palls. It was also proven to be an effective means of developing a fire database for fire-algorithm development and validation in many previous studies (e.g. Li *et al.* 2000a,b). Aided by a geographical information system (ArcGIS, ESRI Inc., Redlands, CA, USA), fire pixels in clusters were integrated into fire events (polygons). In July 2004, there were 5459 fire polygons, 163 being larger than 100 km^2 each. Figure 9 shows a fire polygon containing all fires detected by individual algorithms and by both algorithms. A total of 213 fire pixels detected by MOD-14, denoted by '×', and 432 detected by MOD-MOD, denoted by '+', are shown. Fires detected by both algorithms appear as '∗'. We closely monitored the spread of burn using 42 MODIS granules from 1 to 20 July 2004. Smoke plumes were used as an indicator of burning. Comparing fire hot spots and the presence of smoke confirms that the additional fires detected by MOD-MOD are virtually all true. Yet commission error remains very low, as indicated by the lack of scattered hot spots outside the fire polygon.

Downloaded by [The Nasa Goddard Library] at 10:38 06 September 2012

Downloaded by [The Nasa Goddard Library] at 10:38 06 September 2012

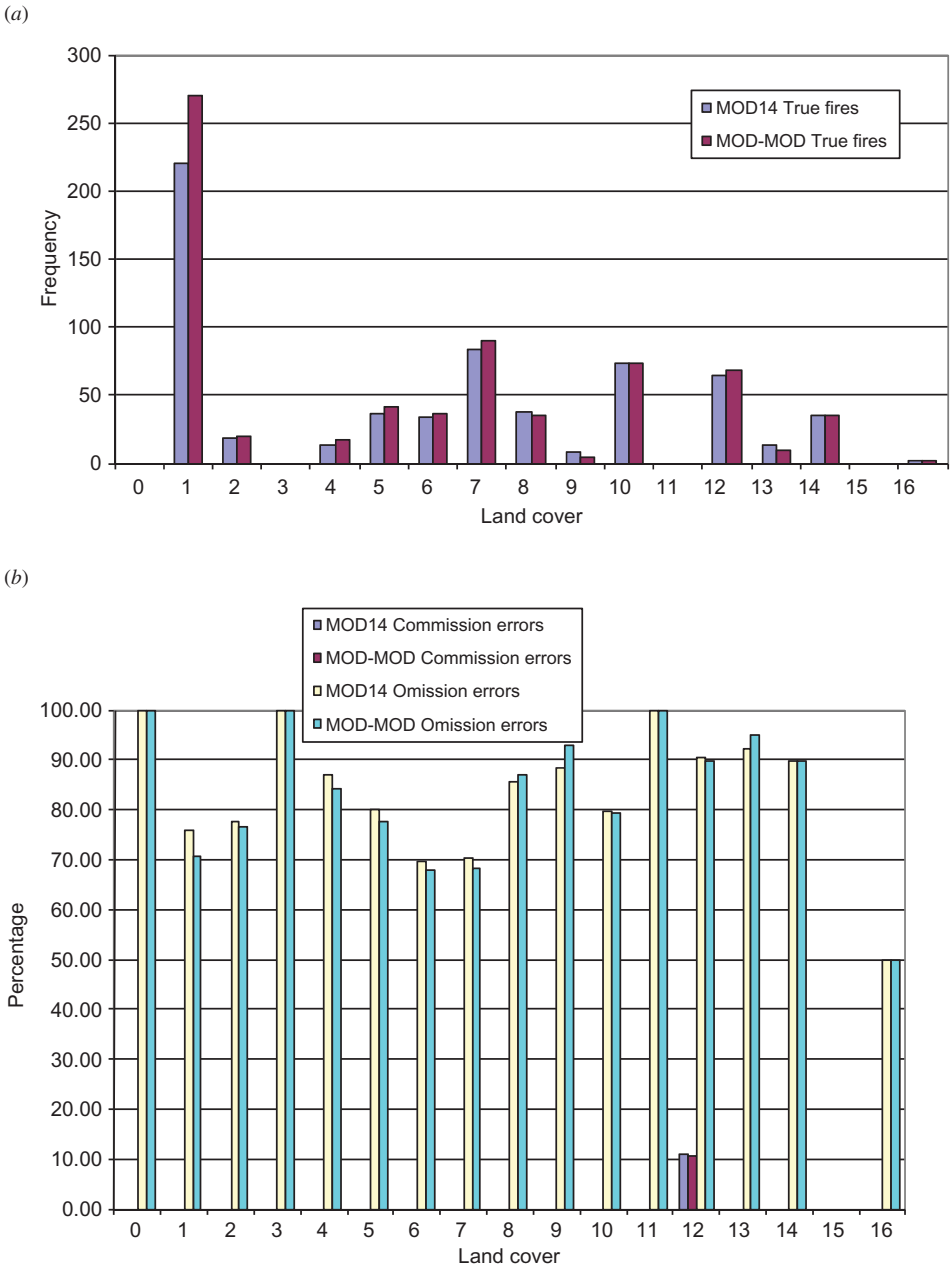

Figure 7. (*a*) The number of true fires detected by applying the two algorithms MOD14 and MOD-MOD to the training datasets and (*b*) their commission and omission errors for various land-cover types.

The improvement by using the MOD-MOD algorithm is highly dependent on land covers. The most significant improvement is made for forest area for which the detection rate is increased by 20% or more, thanks to the changes in difference between $\delta_{T_{4\mathrm{m}}}$ and δ_{T_4} and/or between $\delta_{\Delta T_{\mathrm{m}}}$ and $\delta_{\Delta T}$. These differences are highly dependent on the

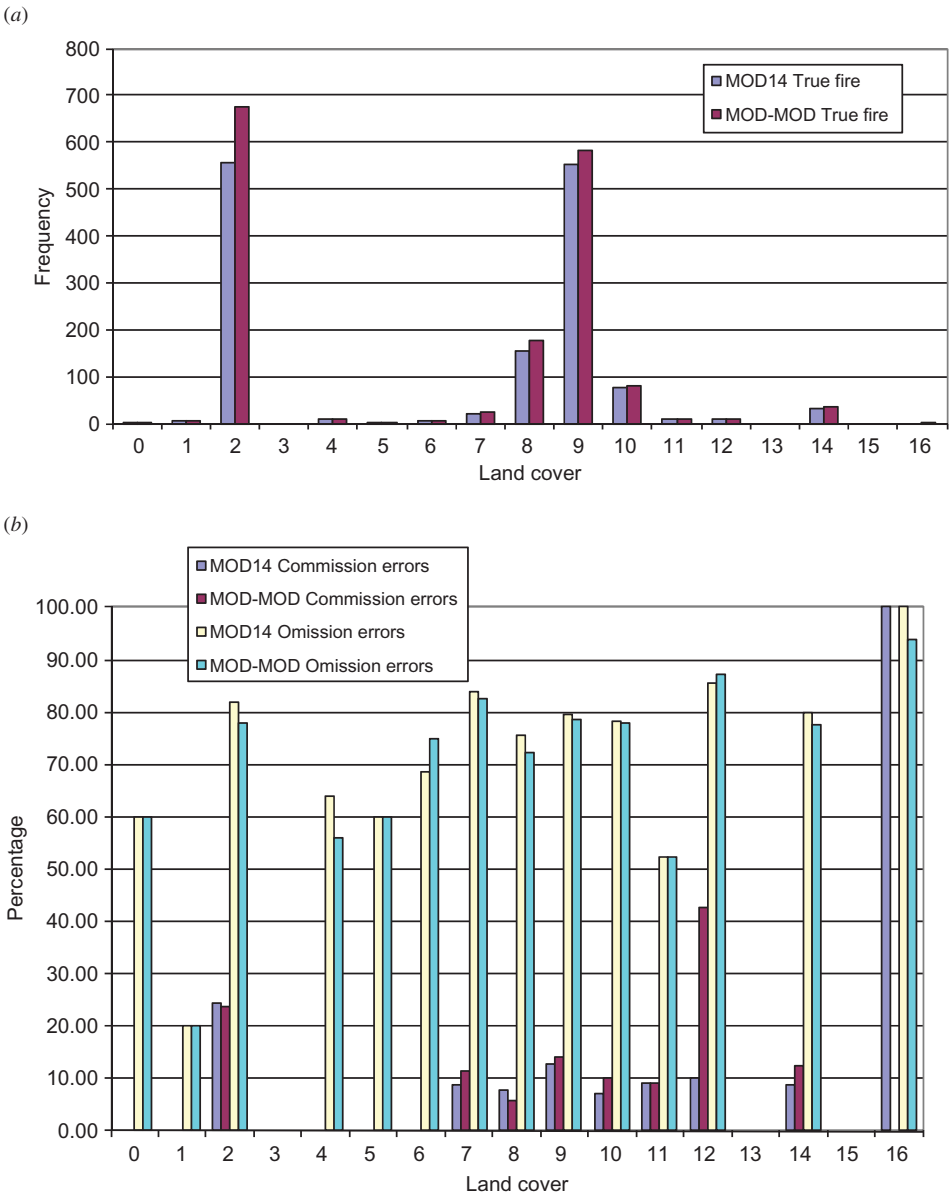

Figure 8. (*a*) The number of true fires detected by applying the two algorithms MOD14 and MOD-MOD to the testing datasets and (*b*) their commission and omission errors for various land-cover types.

heterogeneity of land covers (Li *et al.* 2001). Figures 4 and 5 represent the most ideal conditions under which the land covers of the background are homogeneous (e.g. the most forests), where the magnitudes and their changes in $\delta_{T_{4m}}$ and $\delta_{\Delta T_m}$ after removing the solar contamination are both very small. For some land covers of more heterogeneity and fragmentation, both the magnitudes and differences after removing the solar contamination in $\delta_{T_{4m}}$ and $\delta_{\Delta T_m}$ may be non-negligible. The increases in $3\delta_{T_{4m}}$ and/or

Downloaded by [The Nasa Goddard Library] at 10:38 06 September 2012

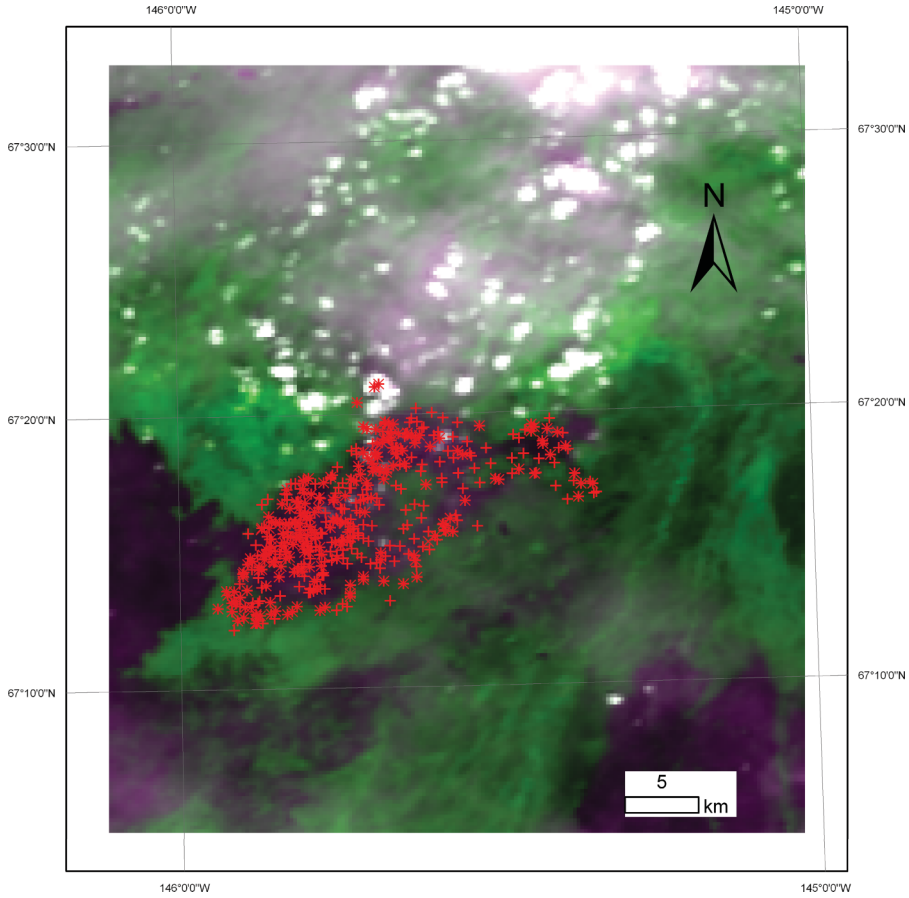

Figure 9. Distribution of fire pixels in a fire event in Alaska. The symbols +, x and * denote fire pixels detected by the MOD-MOD, MOD14 and both algorithms, respectively, from 1 to 20 July 2004, superposed on the 250 m MODIS image of 18 July 2004; the number of fire pixels detected by MOD14 is 213, and the number of fire pixels detected by MOD-MOD is 432.

Downloaded by [The Nasa Goddard Library] at 10:38 06 September 2012

$3.5\delta_{\Delta T_{\mathrm{m}}}$ in equation (12) and/or equation (14) may offset the gain from eliminating solar contamination and have the risk of causing omission errors in the contextual detection. While $\overline{T}_{4\mathrm{m}}$ is decreased, this decrease may be compensated by an increase in $3\delta_{T_{4\mathrm{m}}}$; similarly, decrease in $\overline{\Delta T}_{4\mathrm{m}}$ is compensated by an increase in $3\delta_{\Delta T_{4\mathrm{m}}}$.

Improving the performance of the MOD-MOD algorithm requires fine tuning for any special purposes to meet any special needs for commission and/or omission errors. In our study, fine tuning has two objectives, adapting the algorithm to the modified surface temperatures and achieving the same level of commission error that the MODIS algorithm has.

The improvement of the algorithm is expected to vary with the specific band of the MIR used if it is applied to other sensors. The relative contribution of solar irradiance to the thermal radiation from the background depends highly on the band. This is because solar irradiance changes with wavelength.

5. Concluding remarks

MIR radiances measured by satellite sensors have been widely employed for detecting wildfires due to their high sensitivity to the typical range of fire temperatures (a few hundreds to thousands of degrees). During daytime, MIR radiances include contributions from both thermal emission (the source of the fire signal) and solar reflection (a source of noise). However, solar contamination has yet to be corrected in almost all fire-detection algorithms. In addition, few algorithms account for the contribution of atmospheric thermal path radiance, which varies with the viewing angle.

In this study, radiative transfer in the MIR band is extensively studied in order to remove solar contamination and thermal-path-radiance effects. An LUT was obtained using the MODTRAN4 model for rapid calculation of the two variables. The MODIS emissivity product at 0.05° was resampled to a 0.008333° product with the aid of mid-resolution land-cover data. The MODIS fire-detection algorithm (MOD14) was then modified to account for changes in the brightness temperatures in the MIR band.

A modified fire-detection algorithm (MOD-MOD) was proposed based on the original MODIS fire algorithm by using 81 MODIS granules coincident with 115 ASTER scenes, in the United States from 2002 to 2006. The results were validated against a dataset in Amazonia by matching 135 MODIS granules with 162 ASTER scenes. They were mainly located in the deforestation region of Amazonia from 2000 to 2005. In comparison with the original MODIS fire-detection algorithm, the MOD-MOD algorithm detects 20% more fire pixels for both training and validation data; for the highly limited MODIS fire pixels that could be assessed by ASTER scenes, the MOD-MOD algorithm detects 10% more true fire pixels while maintaining comparable commission errors. The performance of the algorithms in terms of commission and omission errors depends on land covers or regions. Cursory evaluation was also carried out by manually examining fires based on smoke plumes.

Despite discernible improvement, our study still suffers from some problems. A Lambertian surface was assumed, and the resolutions of the datasets employed in the study differ: 5 km for monthly emissivity data and 1 km for the yearly land-cover product and the surface albedo data. Errors are thus incurred due to mismatches in spatial resolutions, different temporal coverage and a lack of angular corrections. Further improvement is expected if better surface albedo/emissivity data are used. The new algorithm also assumes that the background pixels are not seriously altered by fires. In this study, the correction for solar contamination is more precise than the correction for thermal path radiance. Solar contamination is stronger when the path length is shorter (i.e. smaller viewing zenith angle and solar zenith angle), while thermal path radiance is greater when the viewing zenith angle is large.

Although the study is confined to MODIS data, the principles and approach are equally applicable to any other satellite sensors, such as the historical AVHRR and the future GOES-R. The future GOES-R satellite will carry an ABI. It has MIR bands similar to those of MODIS ch21/22. The fire-detection algorithm designed for this sensor would also benefit from the removal of solar contamination and thermal path radiances. It is expected that the elimination of solar contamination in the MIR band for the ABI sensor would have greater effectiveness than that for the MODIS since its MIR band has shorter wavelengths and thus more solar contamination.

Downloaded by [The Nasa Goddard Library] at 10:38 06 September 2012

Acknowledgements

This work was supported by the NOAA's GOES-R Risk Reduction Program. The MODIS L1B and MOD03 geolocation data are available from NASA's level 1 and Atmosphere Archive and Distribution System (http://ladsweb.nascom.nasa.gov/data/). The codes to produce the MODIS fire product (collection 5, version 5.0.1) were downloaded from the NASA direct readout laboratory (http://directreadout.sci.gsfc.nasa.gov/) (Justice *et al.* 2002a). We thank Wilfrid Schroeder for providing the ASTER fire data used in this study.

References

Beringer, J., Hutley, L.B., Tapper, N.J., Coutts, A., Kerley, A. and O'Grady, A.P., 2003, Fire impacts on surface heat, moisture and carbon fluxes from a tropical savanna in northern Australia. *International Journal of Wildland Fire*, **12**, pp. 333–340.

Berk, A., Bernstein, L.S., Anderson, G.P., Acharya, P.K., Robertson, D.C., Chetwynd, J.H. and Adler-Golden, S.M., 1998, MODTRAN cloud and multiple scattering upgrades with application to AVIRIS. *Remote Sensing of Environment*, **65**, pp. 367–375.

Boyd, D.S. and Petitcolin, F., 2004, Remote sensing of the terrestrial environment using middle infrared radiation (3.0–5.0 μm). *International Journal of Remote Sensing*, **25**, pp. 3343–3368.

Csiszar, I. and Sullivan, J., 2002, Recalculated pre-launch saturation temperatures of the AVHRR 3.7 μm sensors on board the TIROS-N to NOAA−14 satellites. *International Journal of Remote Sensing*, **23**, pp. 5271–5276.

Csiszar, I.A., Morisette, J.T. and Giglio, L., 2006, Validation of active fire detection from moderate-resolution satellite sensors: the MODIS example in northern Eurasia. *IEEE Transactions on Geoscience and Remote Sensing*, **44**, pp. 1757–1764.

Flasse, S.P. and Ceccato, P., 1996, A contextual algorithm for AVHRR fire detection. *International Journal of Remote Sensing*, **17**, pp. 419–424.

Friedl, M.A., McIver, D.K., Hodges, J.C.F., Zhang, X.Y., Muchoney, D., Strahler, A.H., Woodcock, C.E., Gopal, S., Schneider, A., Cooper, A., Baccini, A., Gao, F. and Schaaf, C., 2002, Global land cover mapping from MODIS: algorithms and early results. *Remote Sensing of Environment*, **83**, pp. 287–302.

Giglio, L., Descloitres, J., Justice, C.O. and Kaufman, Y.J., 2003, An enhanced contextual fire detection algorithm for MODIS. *Remote Sensing of Environment*, **87**, pp. 273–282.

Giglio, L. and Kendall, J.D., 1999, Evaluation of global fire detection algorithms using simulated AVHRR infrared data. *International Journal of Remote Sensing*, **20**, pp. 1947–1985.

Ichoku, C., Kaufman, Y., Giglio, L., Li, Z., Fraser, R.H., Jin, J. and Park, B., 2003, Comparative analysis of daytime fire detection algorithms using AVHRR data for the 1995 fire season in Canada: perspective for MODIS. *International Journal of Remote Sensing*, **24**, 1669–1690.

Ichoku, C. and Kaufman, Y.J., 2005, A method to derive smoke emission rates from MODIS fire radiative energy measurements. *IEEE Transactions on Geoscience and Remote Sensing*, **43**, pp. 2636–2649.

Jin, Y. and Roy, D.P., 2005, Fire-induced albedo change and its radiative forcing at the surface in northern Australia. *Geophysical Research Letters*, **32**, L13401, doi:10.1029/2005GL022822.

Justice, C.O., Giglio, L., Korontzi, S., Owens, J., Morisette, J.T., Roy, D., Descloitres, J., Alleaume, S., Petitcolin, F. and Kaufman, Y., 2002a, The MODIS fire products. *Remote Sensing of Environment*, **83**, pp. 244–262.

Justice, C.O., Townshend, J.R.G., Vermote, E.F., Masuoka, E., Wolfe, R.E., Saleous, N., Roy, D.P. and Morisette, J.T., 2002b, An overview of MODIS Land data processing and product status. *Remote Sensing of Environment*, **83**, pp. 3–15.

Downloaded by [The Nasa Goddard Library] at 10:38 06 September 2012

Kaufman, Y.J., Justice, C.O., Flynn, L.P., Kendall, J.D., Prins, E.M., Giglio, L., Ward, D.E., Menzel, W.P. and Setzer, A.W., 1998, Potential global fire monitoring from EOS-MODIS. *Journal of Geophysical Research – Atmospheres*, **103**, pp. 32 215–32 238.

Kaufman, Y.J. and Remer, L.A., 1994, Detection of forests using mid-Ir reflectance – an application for aerosol studies. *IEEE Transactions on Geoscience and Remote Sensing*, **32**, pp. 672–683.

Kaufman, Y.J., Tucker, C.J. and Fung, I., 1990, Remote-sensing of biomass burning in the tropics. *Journal of Geophysical Research – Atmospheres*, **95**, pp. 9927–9939.

Kennedy, P.J., Belward, A.S. and Gregoire, J.M., 1994, An improved approach to fire monitoring in West Africa using AVHRR data. *International Journal of Remote Sensing*, **15**, pp. 2235–2255.

King, M.D., Menzel, W.P., Kaufman, Y.J., Tanre, D., Gao, B.C., Platnick, S., Ackerman, S.A., Remer, L.A., Pincus, R. and Hubanks, P.A., 2003, Cloud and aerosol properties, precipitable water, and profiles of temperature and water vapor from MODIS. *IEEE Transactions on Geoscience and Remote Sensing*, **41**, pp. 442–458.

Lasaponara, R., Cuomo, V., Macchiato, M.F. and Simoniello, T., 2003, A self-adaptive algorithm based on AVHRR multitemporal data analysis for small active fire detection. *International Journal of Remote Sensing*, **24**, pp. 1723–1749.

Lee, T.F. and Tag, P.M., 1990, Improved detection of hotspots using the AVHRR 3.7-μm channel. *Bulletin of the American Meteorological Society*, **71**, pp. 1722–1730.

Li, Z., 1998, Influence of absorbing aerosols on the inference of solar surface radiation budget and cloud absorption, *Journal of Climate*, **11**, pp. 5–17.

Li, Z.Q., Cihlar, J., Moreau, L., Huang, F.T. and Lee, B., 1997, Monitoring fire activities in the boreal ecosystem. *Journal of Geophysical Research – Atmospheres*, **102**, pp. 29 611–29 624 .

Li, Z., Nadon, S. and Cihlar, J., 2000a, Satellite-based detection of Canadian boreal forest fires: development and application of the algorithm. *International Journal of Remote Sensing*, **21**, pp. 3057–3069.

Li, Z., Nadon, S., Cihlar, J. and Stocks, B., 2000b, Satellite-based mapping of Canadian boreal forest fires: evaluation and comparison of algorithms. *International Journal of Remote Sensing*, **21**, pp. 3071–3082.

Li, Z., Kaufman, Y., Ithoku, C., Fraser, R., Trishchenko, A., Gilgil, L., Jin, J., Yu, X., Ahern, F., Goldammer, J.G. and Justice, C., 2001, A review of AVHRR-based fire active fire detection algorithm: principles, limitations, and recommendations. In *Global and Regional Vegetation Fire Monitoring from Space, Planning and Coordinated International Effort*, F. Ahern, J.G. Goldammer and C. Justice (Eds.), pp. 199–225 (The Hague, The Netherlands: SPB Academic Publishing).

Masuda, K., Leighton, H.G. and Li, Z., 1995, A new parameterization for the determination of solar flux absorbed at the surface from satellite measurements, *Journal of Climate*, **8**, pp. 1615–1629.

Morisette, J.T., Giglio, L., Csiszar, I. and Justice, C.O., 2005, Validation of the MODIS active fire product over Southern Africa with ASTER data. *International Journal of Remote Sensing*, **26**, pp. 4239–4264.

Nakayama, M., Maki, M., Elvidge, C.D. and Liew, S.C., 1999, Contextual algorithm adapted for NOAA-AVHRR fire detection in Indonesia. *International Journal of Remote Sensing*, **20**, pp. 3415–3421.

Remer, L.A., Kaufman, Y.J., Tanre, D., Mattoo, S., Chu, D.A., Martins, J.V., Li, R.R., Ichoku, C., Levy, R.C., Kleidman, R.G., Eck, T.F., Vermote, E. and Holben, B.N., 2005, The MODIS aerosol algorithm, products and validation. *Journal of the Atmospheric Sciences*, **62**, pp. 947–973.

Rowlands, A. and Sarris, A., 2007, Detection of exposed and subsurface archaeological remains using multi-sensor remote sensing. *Journal of Archaeological Science*, **34**, pp. 795–803.

Downloaded by [The Nasa Goddard Library] at 10:38 06 September 2012

Schroeder, W., Prins, E., Giglio, L., Csiszar, I., Schmidt, C., Morisette, J. and Morton, D., 2008a, Validation of GOES and MODIS active fire detection products using ASTER and ETM plus data. *Remote Sensing of Environment*, **112**, pp. 2711–2726.

Schroeder, W., Ruminski, M., Csiszar, I., Giglio, L., Prins, E., Schmidt, C. and Morisette, J., 2008b, Validation analyses of an operational fire monitoring product: the hazard mapping system. *International Journal of Remote Sensing*, **29**, pp. 6059–6066.

Seemann, S.W., Li, J., Menzel, W.P. and Gumley, L.E., 2003, Operational retrieval of atmospheric temperature, moisture and ozone from MODIS infrared radiances. *Journal of Applied Meteorology*, **42**, pp. 1072–1091.

Tobler, W.R., 1970, A computer model simulation of urban growth in the Detroit region. *Economic Geography*, **46**, pp. 234–240.

Verstraeten, W.W., Veroustraete, F., Van Der Sande, C.J., Grootaers, I. and Feyen, J., 2006, Soil moisture retrieval using thermal inertia, determined with visible and thermal spaceborne data, validated for European forests. *Remote Sensing of Environment*, **101**, pp. 299–314.

Wan, Z.M. and Li, Z.L., 1997, A physics-based algorithm for retrieving land-surface emissivity and temperature from EOS/MODIS data. *IEEE Transactions on Geoscience and Remote Sensing*, **35**, pp. 980–996.

Wang, W.T., Qu, J.J., Hao, X.J., Liu, Y.Q. and Sommers, W.T., 2007, An improved algorithm for small and cool fire detection using MODIS data: a preliminary study in the southeastern United States. *Remote Sensing of Environment*, **108**, pp. 163–170.

Downloaded by [The Nasa Goddard Library] at 10:38 06 September 2012